

Atomistic modeling of nanoscale ferroelectric capacitors using a density functional theory and non-equilibrium Green's-function method

Daniele Stradi*, Ulrik G. Vej-Hansen*, Petr A. Khomyakov*, Maeng-Eun Lee*, Gabriele Penazzi*, Anders Blom*, Jess Wellendorff*, Søren Smidstrup*, and Kurt Stokbro*

*Synopsys Denmark ApS

Fruebjergvej 3, 2100 Copenhagen, Denmark

Email: stradi@synopsys.com

Abstract—We propose a first-principles atomistic method based on density functional theory and the non-equilibrium Green's-function method to investigate the electronic and structural response of metal-insulator-metal capacitors under applied bias voltages. We validate our method by showing its usefulness in two paradigmatic cases where including finite-bias structural relaxation effects is critical to describe the device behavior: formation of dielectric dead layers in a paraelectric SRO|STO|SRO capacitor due to an applied bias voltage, and the switching behavior of a ferroelectric SRO|BTO|SRO capacitor due to an external electric field.

I. INTRODUCTION

With the continuous downscaling of device components, understanding the interplay between electronic and structural response in the presence of an applied electrical bias (V_{bias}) becomes central to determine their functionality. For metal-insulator-metal (MIM) capacitors, the importance of structural effects due to V_{bias} has long been recognized. Atomistic simulations have shown that a significant portion of the capacitance decrease observed in thin paraelectric (PE) perovskite films comes from low-permittivity regions at the metal-insulator interface (“dead layers”) [1], which develop as a result of structural distortions in the insulating layer due to V_{bias} [2]. The behavior of such dead layers beyond the linear-response regime is still poorly understood, possibly due to the lack of atomistic methods that are able to describe the structure of the capacitor at finite V_{bias} [3]. Elucidating the role of V_{bias} in the switching behavior of ferroelectric (FE) materials has also recently become a subject of attention, due to the application of FE-based structures in negative-capacitance field-effect transistors (NC-FETs) [4]. However, similarly to the case of paraelectric MIM capacitors, the atomistic-level description of the switching process is still mostly limited to classical simulations using parametrized Hamiltonians [5] or first-principles methods where other variables than V_{bias} are used to impose an electric field [6]–[8], thereby lacking a direct connection to experimental measurements.

Here, we propose an efficient *ab initio* approach to describe atomistically the electronic and structural response of nanoscale capacitors at finite V_{bias} . Our method accounts for the exact boundary conditions of the capacitor at $V_{\text{bias}} \neq 0$, as well as for the ballistic current between the capacitor plates. These could not be accounted for in previous approaches used to describe finite-bias effects in nanoscale capacitors [8], [9]. We validate our approach by studying the role of V_{bias} in the formation of dead layers in a PE SrRuO₃|SrTiO₃|SrRuO₃ (SRO|STO|SRO) capacitor, and in the FE switching of a SrRuO₃|BaTiO₃|SrRuO₃ (SRO|BTO|SRO) capacitor.

II. METHODOLOGY

All calculations were performed using density functional theory (DFT) and the non-equilibrium Green's-function (NEGF) method, [11] as implemented in the QuantumATK program developed by Synopsys [12], [13]. We used the linear combination of atomic orbitals (LCAO) method and normconserving pseudopotentials (PPs), see [13] for further details.

The SRO|STO|SRO capacitor was based on a thin film made of 7 STO unit cells (UCs), sandwiched between two semi-infinite SRO electrodes. The PBE exchange-correlation functional was used [14], together with PseudoDojo PPs and a PseudoDojo-Medium basis set [10]. The mesh cutoff was 750 Ha. Monkhorst-Pack (MP) k -point grids [15] of 13×13 and $13 \times 13 \times 401$ were used for the device and for the electrodes, respectively. In the MIM structure, the lattice constant in the xy -plane was set to the calculated lattice constant for STO, $a_{\text{STO}} = 3.95 \text{ \AA}$ to simulate pseudomorphic growth on STO substrates. The zero-bias structure was relaxed along the z -direction using a 2-step procedure. First, a SRO|STO|SRO slab was constructed, with 6 SRO UCs on each side of the STO film. The atomic positions of the central part of the slab were optimized along the z -direction, while keeping fixed the 4 SRO UCs closest to the left surface, and treating the 4 SRO UCs closest to the right surface as a rigid body. A device configuration was then created based on the optimized slab geometry. This configuration was further optimized by

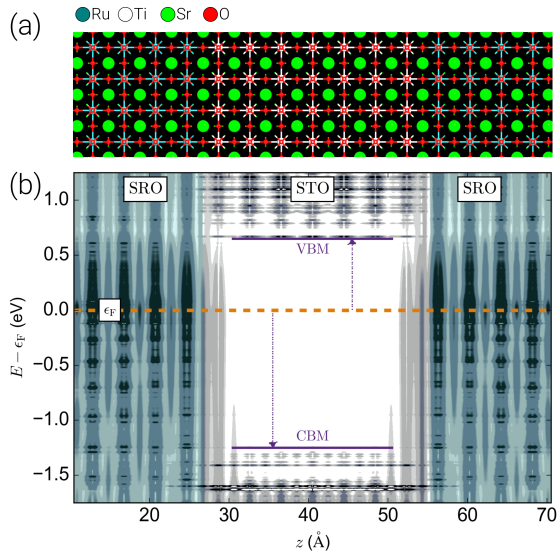


Fig. 1. (a): Structure of the SRO|STO|SRO capacitor. For sake of clarity, the structure has been repeated 4 times in the y direction. (b): PLDOS of the capacitor in (a). Darker (lighter) colors indicate regions of high (low) PLDOS. The shaded blue areas indicate the position of the SRO regions. The solid purple lines mark the position of the CBM and VBM. The orange dashed line marks the position of the Fermi level ϵ_F .

allowing the STO layers and the two SRO layers closest to each surface to relax along z for applied biases in the range $0 \text{ mV} \leq V_{\text{bias}} \leq 100 \text{ mV}$. The threshold for force minimization was $5 \text{ meV}/\text{\AA}$ for all the structural relaxations.

The SRO|BTO|SRO structure was based on a FE thin film made of 9 BTO UCs. The LDA exchange-correlation functional was used, together with FHI PPs and a DZP basis set [10], and a 180 Ha mesh cutoff. 6×6 and $6 \times 6 \times 251$ MP k -point grids were used to sample the BZ of the device and of the electrodes, respectively. The structure at zero bias was optimized using the 2-step procedure described above, with a threshold criterion for the forces of $10 \text{ meV}/\text{\AA}$. Starting from this zero-bias device configuration, we performed a sweep of V_{bias} to investigate the FE behavior of the capacitor. First, we gradually increased V_{bias} up to 300 mV, and optimized the structure of the BTO UCs and of the 2 SRO UCs closest to each interface along z at each intermediate value of V_{bias} . The procedure was then repeated backwards, starting from the structure optimized at 300 mV bias. For each optimized structure, the ballistic current I was calculated by means of the Landauer formula, using a 51×51 MP k -point sampling.

The macroscopic averages [16] of the induced potentials were calculated from the Hartree difference potential, δV_H [13], as $\langle \Delta V_H \rangle = \langle \delta V_H(V_{\text{bias}} \neq 0 \text{ mV}) - \delta V_H(V_{\text{bias}} = 0 \text{ mV}) \rangle$. We calculated the potential drop before ($\langle \Delta V_H^{\text{static}} \rangle$) and after ($\langle \Delta V_H^{\text{rel}} \rangle$) structural relaxation. The depolarization potential was calculated as $\langle \Delta V_H^{\text{dep}} \rangle = \langle \Delta V_H^{\text{rel}} \rangle - \langle \Delta V_H^{\text{static}} \rangle$. The corresponding electric fields in the center of the capacitor were calculated from linear fits to those potentials in the center of the insulating region. For the PE capacitor, the profile

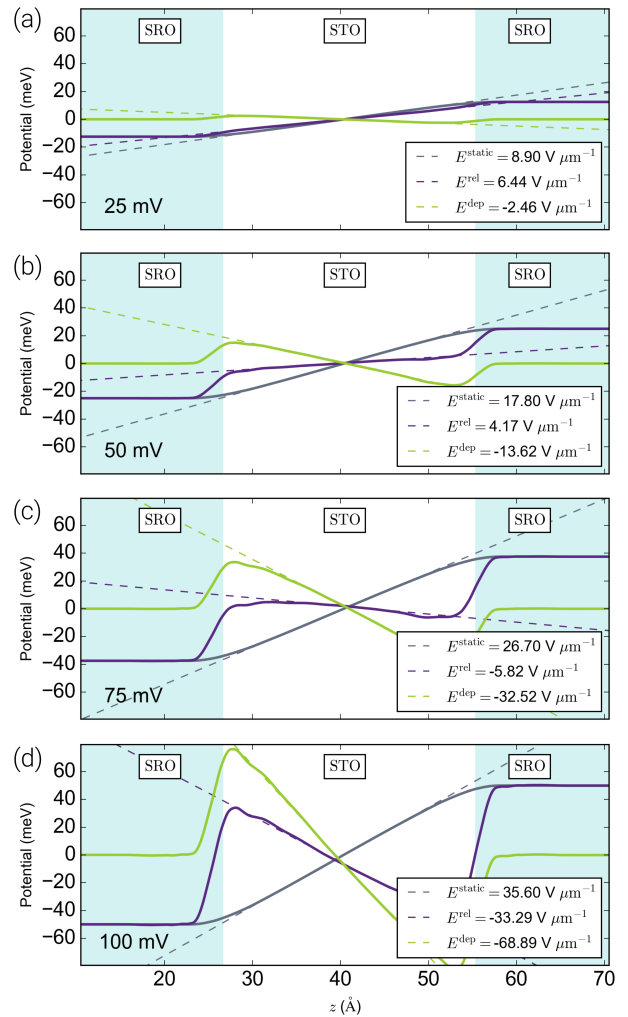


Fig. 2. (a): Macroscopic average of the induced potentials in the SRO|STO|SRO capacitor at $V_{\text{bias}} = 25 \text{ mV}$. The profiles of the potential drop before ($\langle \Delta V_H^{\text{static}} \rangle$) and after ($\langle \Delta V_H^{\text{rel}} \rangle$) structural optimization are shown as grey and purple solid lines, respectively. The depolarization potential ($\langle \Delta V_H^{\text{dep}} \rangle$) is shown as a green solid line. Dashed lines indicate the linear fits in the center of the STO region used to extract the fields associated with each potential. The values of the resulting field are shown in the legend. (b-d): same as (a), but for $V_{\text{bias}} = 50 \text{ mV}$, 75 mV , 100 mV .

of the inverse relative permittivity, $1/\epsilon_r$, was calculated as $1/\epsilon_r = -1/E_{\text{ext}} \times \partial \Delta V_H^{\text{rel}} / \partial z$, where $E_{\text{ext}} = \epsilon E_{\text{int}}$, and $\epsilon = 239$ and E_{int} are the dielectric constant calculated for bulk STO and the internal field in the insulating layer, respectively. The projected local density of states (PLDOS) across the device at zero bias was calculated on a 25×25 MP k -point grid.

III. RESULTS

A. SRO|STO|SRO paraelectric capacitor

The PLDOS of the SRO|STO|SRO PE capacitor in Fig. 1b shows that the SRO electrodes are metallic, while the band gap in the center of the STO film is roughly 2 eV. Close to both SRO|STO interfaces, a finite DOS is present within the

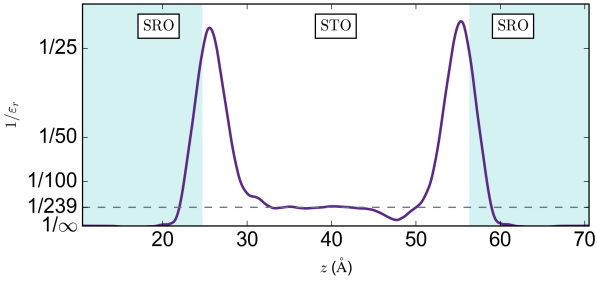


Fig. 3. Profile of the inverse permittivity $1/\epsilon_r$ along the z Cartesian direction of the SRO|STO|SRO capacitor, obtained from $\langle \Delta V_H^{\text{rel}} \rangle$ in Fig. 2b. The dashed grey line marks the value of inverse permittivity $1/239$ calculated for bulk STO.

STO gap, which we identify as metal-induced gap states. The gap states pin the bands of the STO film to the Fermi energy (ϵ_F) of SRO, which results in the STO valence band maximum (VBM) lying about 1.25 eV below ϵ_F , in good agreement with literature results reported for a similar capacitor structure [2].

At $V_{\text{bias}} > 0$, the Ti (O) sublattice of STO translates along (opposite to) the direction of the applied field, indicating a structural distortion along the zone-center optical modes. At $V_{\text{bias}} = 25$ mV, the geometry is only slightly deformed, and the profile of $\langle \Delta V_H^{\text{rel}} \rangle$ closely matches that of $\langle \Delta V_H^{\text{static}} \rangle$, see Fig. 2a. As a result, $\langle \Delta V_H^{\text{dep}} \rangle$ is almost flat, and the depolarization field $E^{\text{dep}} \sim 0$ V/ μm , indicating that the dead layers are not fully developed at this bias voltage. These results differ from those obtained in [2] using a linear-response method, since in that case the formation of dead layers was observed at comparable values of V_{bias} . Increasing further V_{bias} results in a highly nonlinear behavior of the profile of $\langle \Delta V_H^{\text{rel}} \rangle$, which points at the formation of dead layers at the SRO|STO interfaces. At $V_{\text{bias}} = 50$ mV, the profiles of $\langle \Delta V_H^{\text{rel}} \rangle$ and $\langle \Delta V_H^{\text{dep}} \rangle$, shown in Fig. 2b, are qualitatively similar to those reported in [2]. Note that $\langle \Delta V_H^{\text{rel}} \rangle$ is flat in the SRO regions away from the interface, indicating that the field induced by V_{bias} has been fully screened. The presence of dielectric dead layers is even more evident from the inverse permittivity profile in Fig. 3, which shows two peaks at the SRO|STO interfaces, indicating regions of reduced permittivity. The $1/\epsilon_r$ profile is only qualitatively similar to that reported in [2]. In particular, the low-permittivity regions calculated here are considerably sharper, and $1/\epsilon_r$ tends to the correct limit $1/\infty$ close to the metallic electrodes. Furthermore, additional features are resolved, in particular the asymmetry in the $1/\epsilon_r$ profile between the dead layers, which is due to the formation of a dipole caused by the field-induced distortion of the STO lattice. The main reason for these improved results is that the DFT-NEGF method applied here imposes the physically correct boundary conditions on the device. In more quantitative terms, the values obtained here for the fields in the center of the insulating film are roughly twice as large as those obtained at 27.8 mV bias voltage in [2], which supports the numerical accuracy of our DFT-NEGF method.

For $V_{\text{bias}} > 50$ mV, the nonlinear behavior of $\langle \Delta V_H^{\text{rel}} \rangle$ becomes even more pronounced, see Fig. 2c,d. We may assume that the capacitor can be described as three effective capacitors in series, $C = (C_{\text{int}}^{-1} + C_0^{-1} + C_{\text{int}}^{-1})^{-1}$. With $C_0 \sim Q/E^{\text{rel}}d$, and since Fig. 2 shows that E^{rel} becomes negative at $V_{\text{bias}} \geq 75$ mV, our simulations suggest that the SRO|STO|SRO central region acquires a negative effective capacitance ($C_0 < 0$) as the bias voltage is ramped up.

B. SRO|BTO|SRO ferroelectric capacitor

The SRO|BTO|SRO capacitor exhibits a finite polarization \vec{P} in the BTO film, which affects its electronic and electrical properties. Due to the finite \vec{P} , the capacitor behaves as a FE switch, as verified here by electronic-structure analysis and simulated I - V_{bias} characteristics. As shown in Fig. 4, the latter exhibits a clear hysteretic behavior characterized by a low-(LR) and a high-resistance (HR) state, which is a key feature of a FE switch.

The PLDOS shown in Fig. 5a for the LR state at $V_{\text{bias}} = 100$ mV is representative of its electronic structure at $0 \text{ mV} \leq V_{\text{bias}} < 300$ mV. In this bias range, the direction of \vec{P} is along z , *i.e.*, $P_z > 0$. This affects the CBM and VBM throughout the BTO film, which are bent in the opposite direction with respect to \vec{P} , and results in an asymmetric potential barrier, which can be approximated by a trapezoidal shape. For each V_{bias} , we estimated the trapezoidal barrier by performing a linear fit to $\langle V_H \rangle$, and subsequently aligned it with the CBM in the center of the BTO insulator at zero bias. Increasing V_{bias} results in a monotonic increase in the current I , but only in minor changes to the shape of the barrier. The profile of $\langle \Delta V_H^{\text{rel}} \rangle$ in Fig. 5b shows that dead layers appear at the SRO|BTO interfaces, resulting in a sizeable “depolarizing” field in the center of the capacitor. This behavior is fully consistent with that observed above for the PE capacitor. However, in the FE case, $P \neq 0$ at zero bias, and the effect of the dead layers is to inhibit changes in \vec{P} with V_{bias} inside the BTO

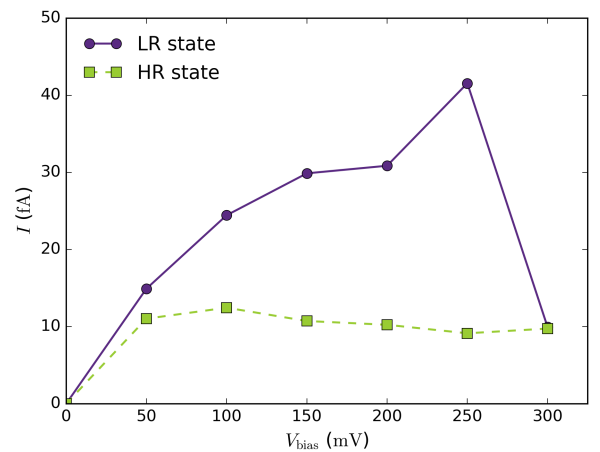


Fig. 4. I - V_{bias} characteristics calculated for the ferroelectric SRO|BTO|SRO capacitor. Solid purple line (circles): low-resistance (LR) state. Green dashed line (squares): high-resistance (HR) state.

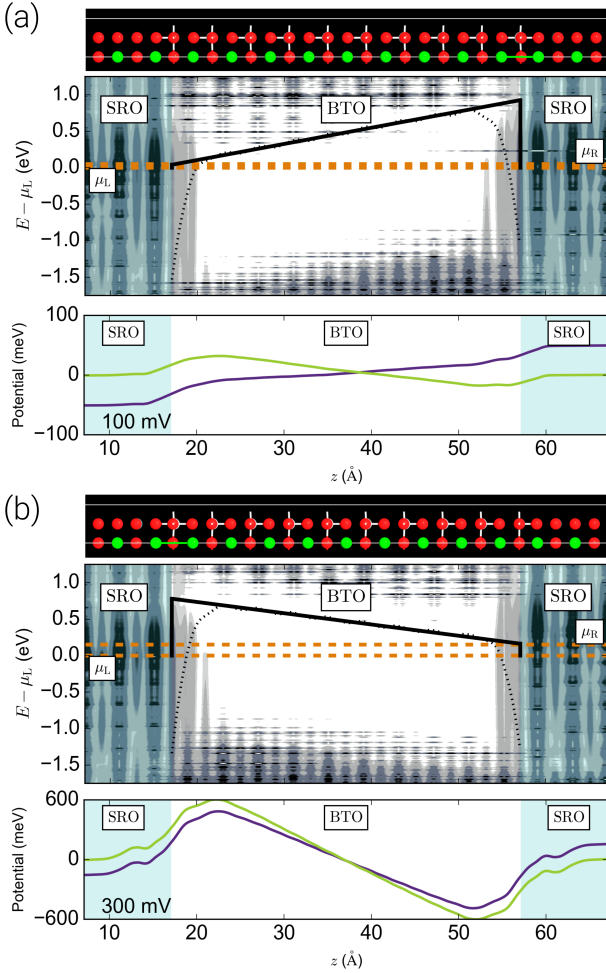


Fig. 5. (a): Low-resistance state of the SRO|BTO|SRO capacitor at $V_{\text{bias}} = 100$ mV. Top panel: structure of the capacitor. Central panel: PLDOS of the capacitor structure in the top panel. The color scheme is the same as in Fig. 1, with the difference that the orange dashes lines indicate the position of the left (μ_L) and right (μ_R) chemical potentials. The dotted line indicates the macroscopic average of the Hartree difference potential $\langle V_H \rangle$. The solid black line indicate the shape of the trapezoidal potential barrier. Bottom panel: profiles of the potential drop $\langle \Delta V_H^{\text{rel}} \rangle$ and of the depolarization potential $\langle \Delta V_H^{\text{dep}} \rangle$. (b): Same as (a) but for the high-resistance state at $V_{\text{bias}} = 300$ mV.

film, resulting in a small variation of the barrier shape with V_{bias} . The increase in the current I is therefore mostly due to the increasingly larger number of states that become available for electron transmission inside the bias window as V_{bias} is increased.

At $V_{\text{bias}} = 300$ mV the polarization of the BTO thin film switches spontaneously to $P_z < 0$. This change in polarization is associated with a sudden drop of I , as seen in Fig. 4. The PLDOS of the resulting HR state in Fig. 5b is representative of its electronic structure at $0 \text{ mV} \leq V_{\text{bias}} \leq 300$ mV. The CBM and VBM are bent in the opposite direction compared to the LR state, resulting in a trapezoidal barrier shape that is now inverted. This suggests that the capacitor behaves as a FE switch, which is irreversibly switched between a LR and a HR state when $V_{\text{bias}} \geq V_C$, $V_C = 300$ mV being the coercive field

required for polarization switching [17]. Indeed, following the LR \rightarrow HR switching event, $I^{\text{HR}} < I^{\text{LR}}$ for each bias voltage as it is decreased towards zero, which confirms the irreversibility of the switching event.

IV. CONCLUSIONS

We have proposed a computational method based on density functional theory and non-equilibrium Green's functions to account for both electronic structure and geometry relaxation effects in MIM capacitors induced by a finite bias voltage. We have shown that the method allows for a straightforward interpretation of complex effects due to field-induced structural relaxation, such as formation of dielectric dead layers and ferroelectric switching. We expect that the method will find broad applicability for complex and technologically relevant capacitor structures beyond those considered in this work, and could be useful to extract fundamental parameters to be used as input for higher-level TCAD tools.

REFERENCES

- [1] C. Zhou and D. M. Newns, "Intrinsic dead layer effect and the performance of ferroelectric thin film capacitors" *J. Appl. Phys.*, vol. 82, p. 3031, 1997.
- [2] M. Stengel and N. A. Spaldin, "Origin of the dielectric dead layer in nanoscale capacitors" *Nature*, vol. 443, pp. 679–682, 2009.
- [3] D. I. Bilc, F. D. Novaes, J. Íñiguez, P. Ordejón, and P. Ghosez, "Electroresistance effect in ferroelectric tunnel junctions with symmetric electrodes" *ACS Nano*, vol. 6, pp. 1473–1478, 2012.
- [4] S. Salahuddin and S. Datta, "Use of negative capacitance to provide voltage amplification for low power nanoscale devices" *Nano Lett.*, vol. 8, pp. 405–410, 2008.
- [5] T. Nishimatsu, U. V. Waghmare, Y. Kawazoe, and D. Vanderbilt, "Fast molecular-dynamics simulation for ferroelectric thin-film capacitors using a first-principles effective Hamiltonian" *Phys. Rev. B*, vol. 78, p. 104104, 2008.
- [6] S. Kasamatsu, S. Watanabe, and S. Han, "First-principles calculation of charged capacitors under open-circuit conditions using the orbital-separation approach" *Phys. Rev. B*, vol. 92, 115124, 2015.
- [7] S. Kasamatsu, S. Watanabe, C. S. Hwang, and S. Han, "Emergence of negative capacitance in multidomain ferroelectric-paraelectric nanocapacitors at finite bias" *Adv. Mater.*, vol. 28, pp. 335–340, 2016.
- [8] M. Stengel, D. Vanderbilt, and N. A. Spaldin, "First-principles modeling of ferroelectric capacitors via constrained displacement field calculations" *Phys. Rev. B*, vol. 80, p. 224110, 2009.
- [9] M. Stengel and N. A. Spaldin, "*Ab initio* theory of metal-insulator interfaces in a finite electric field" *Phys. Rev. B*, vol. 75, p. 205121, 2007.
- [10] S. Kasamatsu, S. Watanabe, and S. Han, "Orbital-separation approach for consideration of finite electric bias within density-functional total-energy formalism" *Phys. Rev. B*, vol. 84, p. 085120, 2011.
- [11] D. Stradi, U. Martinez, A. Blom, M. Brandbyge, and K. Stokbro, "General atomistic approach for modeling metal-semiconductor interfaces using density functional theory and nonequilibrium Green's function" *Phys. Rev. B*, vol. 93, p. 155302, 2016.
- [12] <https://www.synopsys.com/silicon/quantumatk.html>
- [13] S. Smidstrup *et al.*, "QuantumATK: An integrated platform of electronic and atomic-scale modelling tools" arXiv:1905.02794v1.
- [14] J. P. Perdew, K. Burke, and M. Ernzerhof, "Generalized gradient approximation made simple" *Phys. Rev. Lett.*, vol. 77, p. 3865, 1996.
- [15] H. J. Monkhorst and J. D. Pack, "Special points for Brillouin-zone integrations" *Phys. Rev. B*, vol. 13, p. 5188, 1976.
- [16] A. Baldereschi, S. Baroni, and R. Resta, "Band offsets in lattice-matched heterojunctions: A model and first-principles calculations for GaAs/AlAs" *Phys. Rev. Lett.*, vol. 61, p. 734, 1988.
- [17] H. Kohlstedt, N. A. Pertsev, J. Rodriguez Contreras, and R. Waser, "Theoretical current-voltage characteristics of ferroelectric tunnel junctions" *Phys. Rev. B*, vol. 72, p. 125341, 2005.